

Facile synthesis of Fe₃O₄/SiO₂/Cu nanoparticles: investigation of physicochemical attributes of interaction in cationic micellar media and photo-antibacterial impact

M. Darroudi ^a, S. Iftikhar ^b, H. Gaigi ^c, M. B. Taj ^{d*}, S. Noor ^e, N. A. Babteen ^f,
A. M. Alnajeebi ^f, M. Abualnaja ^g, A. Raheel ^h, A. M. Bannunah ⁱ, W. Alelwani ^f

^a Department of Energy Science and Technology, Faculty of Science, Turkish-Germen University, 106 34820, Istanbul, Turkey

^b Department of Chemistry, University of Sahiwal, Sahiwal Pakistan

^c Laboratory of Materials Molecules and Applications, Preparatory Institute of Scientific and Technical Studies, University of Carthage, La Marsa, Tunis, 2070, Tunisia

^d Institute of Chemistry, Division of Inorganic Chemistry, The Islamia University Bahawalpur, Bahawalpur 63100, Pakistan

^e Department of Chemistry, University of Agriculture, Faisalabad, 38040, Pakistan

^f Department of Biochemistry, College of Science, University of Jeddah, Jeddah, Saudi Arabia

^g Department of Chemistry, Faculty of Applied Science, Umm Al-Qura University, Makkah, Saudi Arabia

^h Department of Chemistry, Quaid-e-University Islamabad Campus, Islamabad, 44000, Pakistan

ⁱ Department of Basic Sciences, Common First-year Deanship, Umm Al-Qura University, Makkah, Saudi Arabia

Solubilization of core-shell magnetic nanoparticles has gained new popularity as a versatile partitioning method with the recent growth in nanotechnology and related biotechnology applications. In this sense, Fe₃O₄/SiO₂/Cu nanoparticles (NPs) were designed and characterized by various techniques such as Ultra-violet visible (UV-vis), Fourier transforms infrared (FTIR), X-ray diffractometry (XRD), scanning and transmission electron microscopy (SEM & TEM), energy dispersive X-ray (EDX) and thermogravimetric (TGA) analyses. The size determined by TEM analysis of Fe₃O₄/SiO₂/Cu NPs was found in the range of 24 nm. The diffractometer results verified the impurity-free synthesis of the desired nanoparticles. Micellar solubilization and thermodynamics of micellization were determined correspondingly using a UV-Vis spectrophotometer and conductometer. The thermodynamics of micellization in terms of enthalpy, entropy and standard Gibb's free energy was determined using electrical conductometry. The solubilization parameters viz. partition constant (K_c), binding constant (K_b), partition coefficient (K_v), and the corresponding Gibb's free energies were estimated from the absorption spectroscopic analysis. The experimental outcomes and their computation revealed the rise in the critical micelle concentration of CTAB due to the incorporation of the nanoparticles with the micelles. Moreover, the photo-antibacterial activity of the nanoparticles in the bacteria culture environment showed effectiveness in comparison to the control group.

(Received January 4, 2022; Accepted May 11, 2022)

Keywords: Magnetic nanoparticles, UV-Vis spectroscopy, Electrical conductometry, Micellar solubilization, Antibacterial activity

1. Introduction

To date, many methods of remediation of the industrial effluents have been in practice, but the methods based on biological, physical, and chemical treatments are very common[1]. The methods such as photocatalytic degradation, membrane process, reverse osmosis, ozonation, oxidation, photo-Fenton and electrochemical procedures have been extensively employed for remediation[2]. Most of these above-mentioned methods have some restrictions except photocatalytic degradation which acts as a very handy and smart tool due to being simple, efficient, and inexpensive[3]. Moreover, it could be operated under ambient conditions, and it has excellent biological and chemical sensing and minimal formation of byproducts. Among the many approaches to improving water and food quality against microbial agents, the use of nanoparticles has emerged on the horizon to contribute to this field[4]. Nowadays, the use of copper-containing semiconductor nanoparticles as photocatalysts for disinfection and purification of industrial and domestic effluents is due to its low cost, easy availability, chemical stability, anti-bacterial property and exceptional photocatalytic potential to degrade recalcitrant organic pollutants[5, 6]. With the irradiation of photocatalysts with suitable light sources various reactive species such as superoxides, and hydroxyl radicals along with photo-generated electrons and holes are generated which can cause the deactivation of microorganisms[7]. Previously reported results by some researchers have shown that bare copper nanoparticles showed weak photocatalytic activity under visible light sources and had a narrow light-response range[8]. With the incorporation of copper in a suitable nanosystem, the photocatalytic performance, and separation efficiency of electron-hole pairs could be improved during the photocatalytic process[9]. The incorporation of the silicon oxide layer between the photocatalyst shell and the magnetic core prevents the recombination of electrons (e^-) and holes (h^+)[10]. This could decline the negative effects of Fe_3O_4 on the photocatalytic process of Cu, retain the magnetic properties, prevent oxidation of Fe_3O_4 , and enrich the antibacterial efficiency[11].

Considering the biological applications of magnetic nanoparticles, the study of micellar interaction is of much importance[12]. Surfactants are amphiphilic moieties that form colloidal size micelles to facilitate the solubilization of insoluble or sparingly soluble substances in aqueous media[13, 14]. The dynamic phenomenon of solubilization plays many key functions during biological and industrial processes[15]. Various industries, especially the textiles and pharmaceutical sector are expediting the research on the role of surfactant interactions with the help of models, procedures, and techniques[16, 17].

In this study, our research group managed to synthesize $Fe_3O_4/SiO_2/Cu$ NPs and studied the interactions in the cationic micellar media of CTAB (cetyltrimethylammonium bromide) along with the photo antibacterial activity.

2. Experimental details

From Sigma Aldrich all reagents were purchased and were used without further purification. FTIR Bruker spectrometer (Bruker Tensor 27 FTIR) for the recording of IR spectra. The data were collected in the range of 400 to 4000 cm^{-1} . The crystallite size was measured by

Bruker D8 Advance Powder x-ray Diffractometer with high-resolution LynxEye detector and Cu radiation source. Scanning Electron Microscope (SEM) Philips XL-30E was employed to observe the morphology of nanoparticles. The samples were carbon coated and their morphology was probed using SEM working at an operating voltage of 20 kV. The composition of the material was determined by energy-dispersive X-ray (EDX) spectroscopy. In the case of Transmission Electron Microscopy (TEM) images, the suspensions were dropped onto copper grids; the ethanol was eliminated via the freeze-drying technique; the specimens were subjected to morphological observations on a Transmission Electron Microscope (Philips EM208) with an accelerating voltage of 100 kV.

2.1. Preparation of Fe₃O₄/SiO₂/Cu NPs

2.1.1. Synthesis of Fe₃O₄ NPs

First, the solution was made by dissolving 1g of polyvinyl alcohol (PVA 15000) as a surfactant and 4.8 mmol FeCl₂.4H₂O in 15 mL of water followed by 4.8 mmol of FeCl₃.6H₂O. The stirring was done at 80°C for half an hour, followed by the drop-wise addition of hexamethylenetetramine (HMTA; 1 mol/L) with vigorous stirring to obtain a black solid at pH 10. The black product was immediately filtered, washed with ethyl alcohol, and then dried at 85 °C for 7 h.

2.1.2. Synthesis of Fe₃O₄/SiO₂ NPs

The Fe₃O₄/SiO₂ NPs have been synthesized by a modified Stober method [18]. In a 55 mL mixture of deionized water and ethanol (1:10), the 2.1 mmol of Fe₃O₄ NPs and 0.2 mL of tetraethoxysilane (TEOS) were added followed by 5 mL of NaOH (10 % wt). The product (Fe₃O₄/SiO₂ NPs) was separated after 30 min, stirring at ambient temperature. The product was immediately washed with ethyl alcohol and then dried at 85 °C for 7 h.

2.1.3. Synthesis of Fe₃O₄/SiO₂/Cu NPs

To synthesize Fe₃O₄/SiO₂/Cu NPs, 50 mg of Fe₃O₄/SiO₂ NPs was dispersed in a 50 mL mixture of MeOH/ H₂O (85:15). The pH was maintained at 4.5 by adding 1M HCl. The solution was placed in an ultrasonic bath for 2 h. After that 0.5 mmol of N-[(3-trimethoxysilyl) propyl] ethylenediamine tri acetic acid was added along with a few drops of glacial acetic acid. The complete reaction mixture was again placed in the ultrasonic bath for 2h. The product was precipitated from the reaction mixture using a super magnet followed by acetone washing and then dried in a vacuum at room temperature for 30 min to obtain modified Fe₃O₄/SiO₂ NPs. Afterwards, the CuCl and modified Fe₃O₄/SiO₂ NPs in the equimolar ratio were added to deionized water and stirred for 3 h. The resulting product was separated using a magnet and washed successively with water (10 mL) and ethyl alcohol (10 mL) to get rid of any unreacted CuCl. The product was finally dried in a vacuum at room temperature to yield the Fe₃O₄/SiO₂/Cu NPs.

2.2. Solubilization study

2.2.1. Electrical conductivity to estimate thermodynamic parameters

The thermodynamics of micellization (entropy, enthalpy, Gibb's free energy) were calculated from the conductivity data of CTAB in the presence and absence of nanoparticles under study. The conductivity of all the solutions was recorded on a Hanna conductivity meter (HI-99301; USA) at three different temperatures viz. 298K, 308 K, 318 K. The electrode coated with platinum black was used to minimize and avoid polarization within a range of 0.01 $\mu\text{S}/\text{cm}$ to 199.9 mS/cm. The electrode was initially calibrated using standard potassium chloride solution within the required concentration range [19, 20].

2.2.2. UV-Visible spectroscopy to estimate partition and binding parameters

The absorptions of aqueous and micellar solutions were measured with a double beam UV-Visible spectrophotometer (Perkin Elmer, USA). The absorption scanning and spectrum solutions in the absence and presence of $\text{Fe}_3\text{O}_4/\text{SiO}_2/\text{Cu}$ NPs were observed. After an initial screening of $\text{Fe}_3\text{O}_4/\text{SiO}_2/\text{Cu}$ NPs absorption, the absorption maxima were compared to foresee the extent of micellar interaction. Once the interaction was verified from the comparative absorption values (λ_{max}), the critical micelle concentration was monitored for varying CTAB concentrations. The simple and differential absorption spectra were recorded to estimate the extent of interaction. While measuring simple absorption, the reference was distilled water, whereas the stock solution of $\text{Fe}_3\text{O}_4/\text{SiO}_2/\text{Cu}$ NPs was the reference. In both cases, the micellar solution of $\text{Fe}_3\text{O}_4/\text{SiO}_2/\text{Cu}$ NPs was taken in the sample cells.

2.3. Photo antibacterial activity

The effectiveness of the synthesized nanoparticles was determined by their photocatalytic ability to decolorize bacterial strains. We selected the bacterial strains of *Staphylococcus aureus* (ATCC-6538; Gram-positive), and *Escherichia coli* (ATCC-25922; Gram-negative) to carry out pure culture investigation. The bacteria were inoculated by sterile aliquots of Mueller-Hinton broth (5 ml) followed by overnight incubation at 37°C. After the centrifugation of the samples and these were washed with phosphate buffer saline (PBS) and their concentration was adjusted appropriately. The effect of $\text{Fe}_3\text{O}_4/\text{SiO}_2/\text{Cu}$ NPs on bacterial strains was evaluated by suspending the nanoparticles in Mueller-Hinton broth (2% w/w). The growth of the culture medium was also compared with the photocatalysts. Mueller-Hinton broth inoculated with bacteria served as the positive control. The sterile Microtubes were filled with 0.5 ml of stock solutions and the final concentration was made up to 1 mg/mL, followed by the addition of bacterial suspensions to each Microtube (approx. 105 colony-forming units/mL). The prepared systems were categorized into three sets, the first set was exposed to a UV light source (50W) for 16 min and the samples were drawn from the mixture at various time intervals viz. 0, 2, 4, 8, and 16 min. The second set was subjected to the visible light source (Xenon lamp) and the third set was left without any light source for 160 min the samples from these two groups were taken at intervals of 0, 20, 40, 80, and 160 min. The serial dilutions of the bacterial culture aliquots were prepared in PBS and the colony-forming number of viable cells (CFU/ml) was assessed by the pouring plate technique. All the measurements were observed in triplicate.

3. Results and discussion

The path used to synthesize the $\text{Fe}_3\text{O}_4/\text{SiO}_2/\text{Cu}$ NPs is given in Fig. 1, where TEOS is a tetraethoxysilane molecule and TET is N-[(3-trimethoxysilyl) propyl] ethylenediamine tri acetic acid molecule.

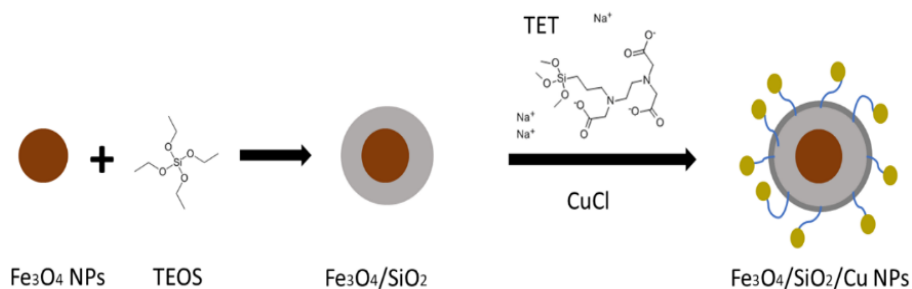


Fig. 1. Preparation of $\text{Fe}_3\text{O}_4/\text{SiO}_2/\text{Cu}$ NPs.

3.1. UV-vis measurements

Fig. 2 represent the UV-vis absorption spectra of Fe_3O_4 NPs with and without a SiO_2 as well as $\text{Fe}_3\text{O}_4/\text{SiO}_2$ NPs decorated by Copper. No obvious peaks were observed in the spectrum of Fe_3O_4 NPs. However, the presence of SiO_2 caused the appearance of a peak at 265 nm in the spectra of the $\text{Fe}_3\text{O}_4/\text{SiO}_2$ NPs. This peak may originate from the changes in the bandgap caused by the quantum size effect and surface effect of SiO_2 NPs[21], as well as from the Fe–O–Si bonds of the core-shell NPs[21]. Moreover, decorated $\text{Fe}_3\text{O}_4/\text{SiO}_2$ NPs with Cu (I) caused the appearance of a broad peak around 600 nm, which originates from the copper NPs[22]. Interestingly, the peak at 250 nm, which was visible in the UV-vis spectrum of $\text{Fe}_3\text{O}_4/\text{SiO}_2$ NPs, was also shifted in $\text{Fe}_3\text{O}_4/\text{SiO}_2/\text{Cu}$ NPs suggesting the presence of Cu (I) which caused changes in the Fe–O–Si bonds.

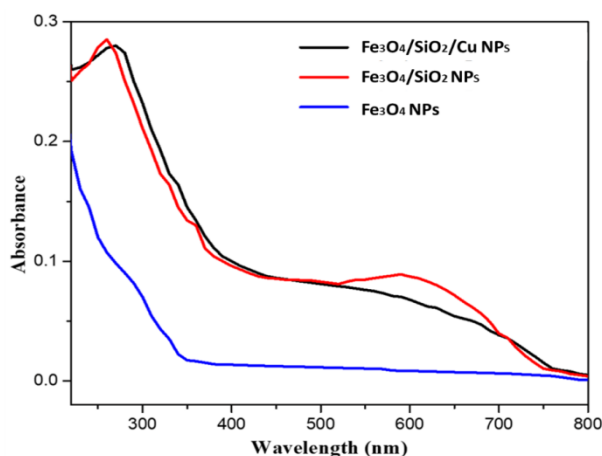


Fig. 2. UV-vis spectra of Fe_3O_4 NPs (blue color), $\text{Fe}_3\text{O}_4/\text{SiO}_2$ NPs (red color) and $\text{Fe}_3\text{O}_4/\text{SiO}_2/\text{Cu}$ NPs (black color).

3.2. FTIR spectroscopy

Fig. 3 represent the FTIR spectra of (a) Fe_3O_4 NPs, (b) $\text{Fe}_3\text{O}_4/\text{SiO}_2$ NPs and (c) $\text{Fe}_3\text{O}_4/\text{SiO}_2/\text{Cu}$ NPs. The characteristic peaks at 3439 and 551 cm^{-1} and 572 cm^{-1} are related to Fe–O which confirms the existence of Fe_3O_4 NPs. The FTIR data for $\text{Fe}_3\text{O}_4/\text{SiO}_2/\text{Cu}$ NPs (Fig. 2b) shows two peaks at 1660 and 1385 cm^{-1} which are attributed to C=O and C-N groups of ligands, respectively and stretching vibration of Si–O appears at 1050, 1110 cm^{-1} . In the FTIR spectrum for $\text{Fe}_3\text{O}_4/\text{SiO}_2/\text{Cu}$ NPs (Fig. 2c), the appearance of a peak at 603.61 cm^{-1} was assigned to Cu–O stretching vibration.

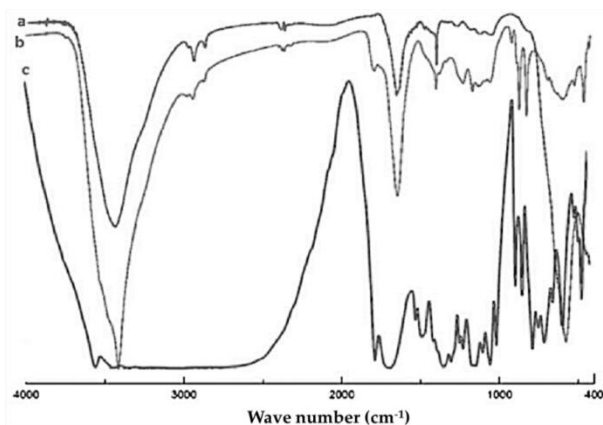


Fig. 3. FTIR spectra of (a) Fe_3O_4 NPs, (b) $\text{Fe}_3\text{O}_4/\text{SiO}_2$ NPs and (c) $\text{Fe}_3\text{O}_4/\text{SiO}_2/\text{Cu}$ NPs.

3.3. SEM results

The field emission scanning electron microscopy (SEM) image in Fig. 4 clearly shows the aggregated morphology of $\text{Fe}_3\text{O}_4/\text{SiO}_2/\text{Cu}$ NPs. It could be considered that copper species are smoothly immobilized on the $\text{Fe}_3\text{O}_4/\text{SiO}_2$ NPs surface. The mean size of the nanoparticles is 25.3 nm. The EDX analysis confirms the presence of desired components (Fe, Si, and Cu) in the $\text{Fe}_3\text{O}_4/\text{SiO}_2/\text{Cu}$ NPs.

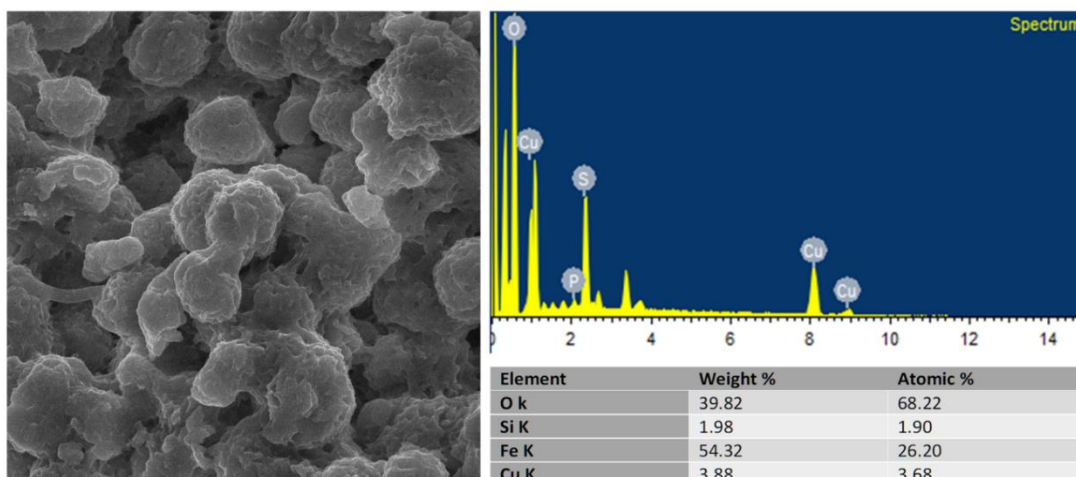


Fig. 4. Fe-SEM images of $\text{Fe}_3\text{O}_4/\text{SiO}_2/\text{Cu}$ NPs and the corresponding EDX spectrum.

3.4. HR-TEM results

As seen in TEM images (Fig. 5), Fe_3O_4 NPs (A) appear spherical while $\text{Fe}_3\text{O}_4/\text{SiO}_2$ NPs (B) it can be seen clearly that Fe_3O_4 NPs are covered with silica coatings. $\text{Fe}_3\text{O}_4/\text{SiO}_2/\text{Cu}$ NPs (C) appear roughly spherical having an average diameter of around 24 nm. The aggregation of nanoparticles may be due to strong interactions between the particles.

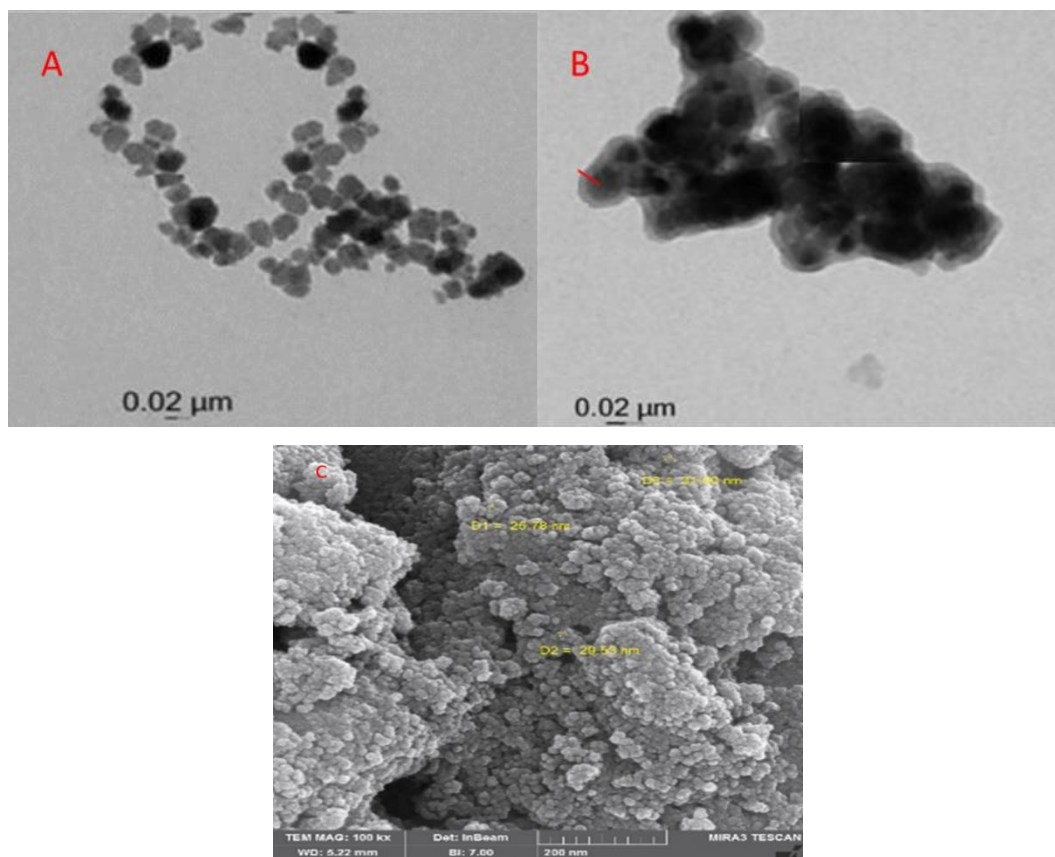


Fig. 5 TEM images of (A) Fe_3O_4 NPs, (B) $\text{Fe}_3\text{O}_4/\text{SiO}_2$ NPs and (C) $\text{Fe}_3\text{O}_4/\text{SiO}_2/\text{Cu}$ NPs

3.5. X-ray diffraction analysis

The X-ray diffraction (XRD) pattern shows characteristic peaks ($2\theta = 43, 52,$ and 74.5) of Cu (I) as shown in Fig. 6. The XRD was investigated with GNR-MPD 3000 in 2θ 10_{-80} at 40 kV that was proved the presence of nanoparticles such as Fe_3O_4 ($2\theta = 29$ (220), 35 (311), 42.5 (222), 54 (511) and 61 (440)) and SiO_2 ($2\theta = 20$). The average size of the nanoparticles was 16.5 nm, calculated by the Debye Scherrer equation.

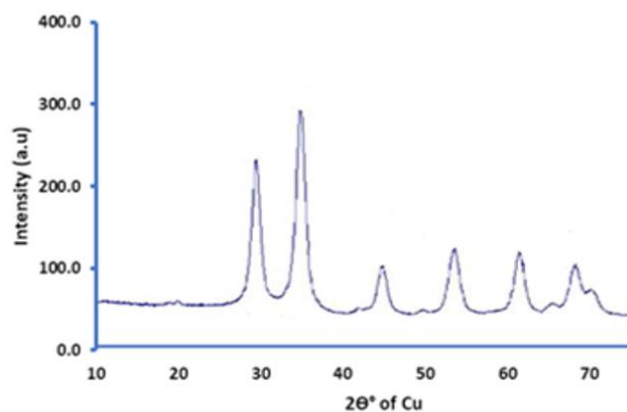


Fig. 6. PXRD pattern of the $Fe_3O_4/SiO_2/Cu$ NPs.

3.6. Thermogravimetric analysis

The TGA curves of $Fe_3O_4/SiO_2/Cu$ NPs are shown in Fig. 7. The TGA analysis was applied to investigate the thermal stability of $Fe_3O_4/SiO_2/Cu$ NPs. The decomposition was in several steps, which the first stage shows the evaporation of water that is physically absorbed on the surface of the nanoparticle and the second stage might be related to the removal of organic moiety involved in the synthesis process. The total weight loss calculated is 9.714 %.

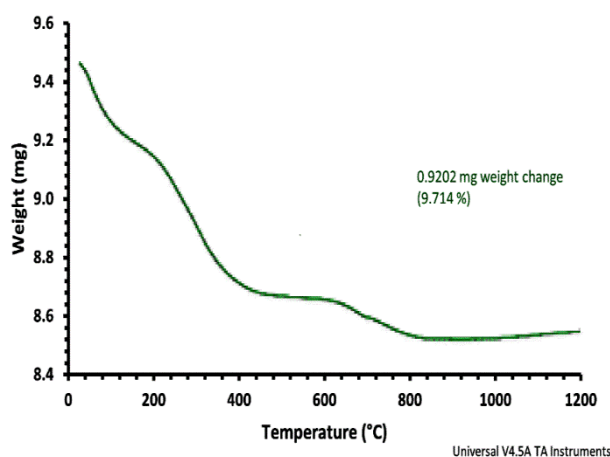


Fig. 7. TGA graph of $Fe_3O_4/SiO_2/Cu$ NPs.

3.7. Estimation of thermodynamics of micellization

Electrical conductivity was employed to estimate the thermodynamic and micellar parameters due to their reliability and sensitivity. On micelle formation, some noticeable change was observed in the electrical conductivity and critical micelle concentration was located at the intersectional point of pre-micellar and post-micellar straight lines in the conductivity-concentration plot, as shown in Figure 8, which represents conductivity-concentration plots of $Fe_3O_4/SiO_2/Cu$ NPs in the presence of CTAB at varying temperatures. The thermodynamic attributes were estimated from conductivity data using equations 1-4.

(a) Extent of ionization

$$\alpha = \frac{S_2 (\text{post-micellar slope})}{S_1 (\text{pre-micellar slope})} \quad (1)$$

(b) Gibb's free energy of micellization

$$\Delta G_m^\circ = (2 - \alpha)RT \ln X_{CMC} \quad (2)$$

(c) The entropy of micellization

$$\Delta S_m = \frac{\Delta H_m - \Delta G_m^\circ}{T} \quad (3)$$

(d) Enthalpy of micellization

$$\Delta H_m = -2.3(2 - \alpha)RT^2 \left[\frac{\partial(\log X_{CMC})}{\partial T} \right]_P \quad (4)$$

In above equations: $X_{CMC} = CMC/55.5$; R = universal gas constant ($\sim 8.314 \text{ J mol}^{-1} \text{ K}^{-1}$); T = absolute temperature.

The thermodynamic parameters calculated at varying temperatures are summarized in Table 1. The experimental findings have supported our hypothesis of micellar solubilization of $\text{Fe}_3\text{O}_4/\text{SiO}_2/\text{Cu}$ NPs in the presence of CTAB and there was a rise in CMC as compared to pure CTAB. The value CMC of pure CTAB (0.9 mM) increased to 0.914 mM in the presence of $\text{Fe}_3\text{O}_4/\text{SiO}_2/\text{Cu}$ NPs and this verified the interaction between the surfactant and nanoparticles. Structure breaking effect of copper in $\text{Fe}_3\text{O}_4/\text{SiO}_2/\text{Cu}$ NPs and carbonyl functionality lead to significant interaction with CTAB. The ion-pair formation of a positively charged headgroup of CTAB and negatively charged carbonylic oxygen could be the plausible reason behind the change in the CMC as compared to pure surfactant solution. This pattern of adsorption made entropy of micellization less convenient and hence micelle formation started at higher concentrations, thus the value of CMC increased.

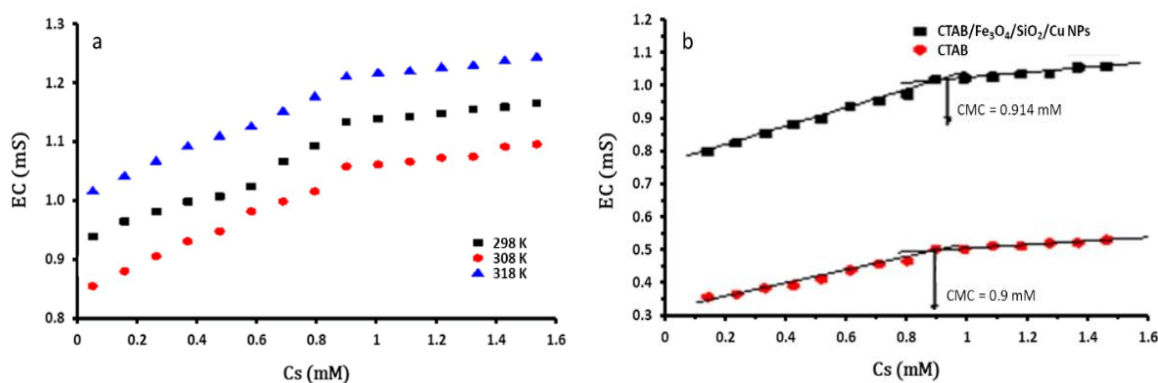


Fig. 8. (a) Plots showing the effect of temperature on electrical conductivity against CTAB concentration (C_s); (b) Comparative plots of conductivity against CTAB concentration (C_s) in an aqueous and micellar solution of $\text{Fe}_3\text{O}_4/\text{SiO}_2/\text{Cu}$ NPs at 298K.

Table 1. Thermodynamic parameters $Fe_3O_4/SiO_2/Cu$ NPs in micellar media of CTAB.

T(K)	CMC (mM)	ΔG_m (kJmol ⁻¹)	ΔH_m (kJmol ⁻¹)	ΔS_m (Jmol ⁻¹ K ⁻¹)	α
298	0.9*	-45.98	-1.43	149.53	0.32
298	0.914	-48.07	-1.36	156.73	0.39
308	0.929	-45.34	-1.60	142.02	0.24
318	0.936	-51.68	-1.72	157.12	0.22

*pure CTAB at 298 K

The relationship between temperature and CMC is not easy to understand. With the temperature rise, there occurs dehydration from the hydrophilic part of micelles facilitates micellization. On the contrary, the dehydration from hydrophobic parts of micelles increases the entropy which in turn disfavors micellization and it occurs at higher CMC. The thermodynamics attributes of micellization are presented in Table 1. The negative magnitudes of Gibb's free energy and entropy of micellization indicated the spontaneity of the $Fe_3O_4/SiO_2/Cu$ NPs/CTAB system. The involvement of hydrophobic and electrostatic interactions was responsible for the system's stability and spontaneity. The exothermicity of the micellar system was indicated by the negative magnitude of ΔH_m . The continuously rising negative value of enthalpy revealed greater hydration of polar groups than the structure breaking effect of water molecules in the vicinity of hydrophobic moieties.

3.8. UV-Visible spectroscopic study

Absorption spectra of $Fe_3O_4/SiO_2/Cu$ NPs in the aqueous and micellar media were recorded at 298 K. The absorption maxima (λ_{max}) of $Fe_3O_4/SiO_2/Cu$ NPs were spotted at 454 nm in aqueous media and this wavelength was used for subsequent absorption analysis. A shift of λ_{max} was critical in deciding the extent of interaction of $Fe_3O_4/SiO_2/Cu$ NPs with CTAB. The hydrophobic force and electrostatic interactions pushed $Fe_3O_4/SiO_2/Cu$ NPs to re-adjust and relocate themselves within micelles. The gradual rise in the absorption with increasing CTAB concentration was observed, possibly due to the significant incorporation of $Fe_3O_4/SiO_2/Cu$ NPs in the micelles and its CMC value shifted from 0.9 mM to 0.917 mM (Fig. 9). The CMC obtained from UV-vis absorption data (0.917 mM) and conductivity data (0.914 mM) agreed. The slight difference in the values was mainly due to their different working principles of the techniques, and secondly, the values CMC is fixed rather it can be found within a certain concentration range between pre-and post-micellar regions.

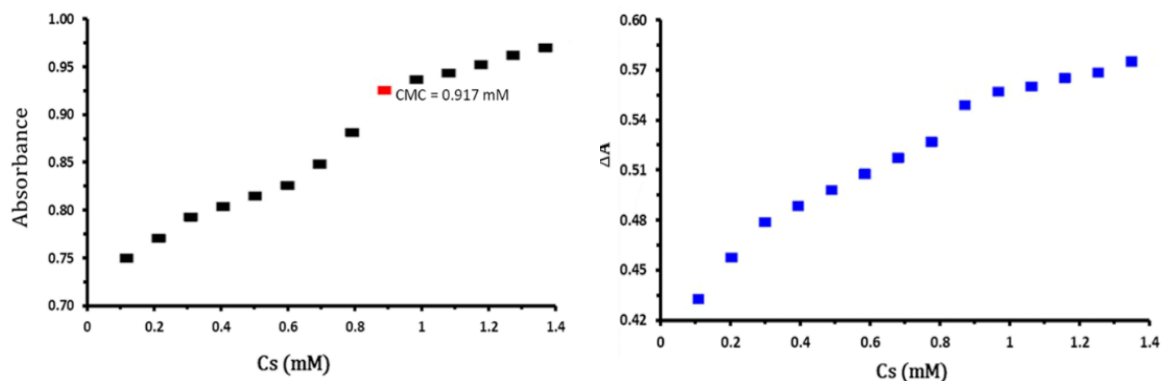


Fig. 9. Plots of $Fe_3O_4/SiO_2/Cu$ NPs/CTAB system Vs CTAB concentration (a) simple absorbance (b) differential absorbance.

Differential spectroscopy was employed for quantitative and qualitative interpretation of micellar interactions. It facilitates estimating binding, partitioning constants, and their corresponding free energy changes. A similar trend was observed in differential absorbance based on gradual and continuous inclusion of $Fe_3O_4/SiO_2/Cu$ NPs within CTAB micelles, as depicted in Fig. 10b. Kawamura devised a model to estimate the partition constant (K_c) and partition coefficient (K_x) are given in equations 5 and 6 [23] and the other parameters were calculated using the following equations (5-9).

$$(a) \quad \text{Partition constant } (K_c): \frac{1}{\Delta A} = \frac{1}{K_c \Delta A_\infty (C_a + C_s^{m_0})} + \frac{1}{\Delta A_\infty} \quad (5)$$

$$(b) \quad \text{Partition coefficient: } K_x = K_c n_w \quad (6)$$

(c) Standard change in Gibb's free energy of partition:

$$\Delta G_p = -RT \ln K_x \quad (7)$$

$$\text{Binding constant } (K_b): \frac{C_s C_a}{\Delta A} = \frac{C_s}{\Delta \epsilon l} + \frac{1}{K_b \Delta \epsilon l} \quad (8)$$

(d) Standard change in Gibb's free energy of binding:

$$\Delta G_b = -RT \ln K_b \quad (9)$$

In the above equations: ΔA = differential absorbance; K_c = partition constant; K_x = partition coefficient; C_a = concentration of $Fe_3O_4/SiO_2/Cu$ NPs; ΔA_∞ = differential absorbance at infinite dilution; $C_s^m = C_s - CMC_0$; C_s = concentration of CTAB, n_w = number of moles of H_2O per liter. Plots to calculate partition and binding constants are given in Figure 10 while their corresponding numerical values are given in Table 2.

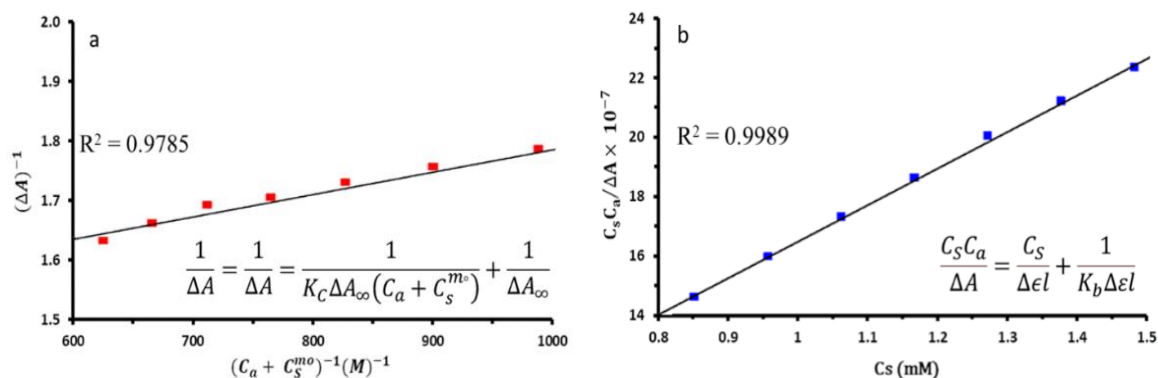


Fig. 10. Graphical representation of (a) Partition constant (K_c); (b) Binding constant (K_b).

Table 2. Solubilization parameters of Fe₃O₄/SiO₂/Cu NPs in the micellar media of CTAB.

$K_c \times 10^{-3}$ (dm ³ mol ⁻¹)	$K_x \times 10^{-3}$	ΔG_p (kJmol ⁻¹)	$K_b \times 10^{-3}$ (dm ³ mol ⁻¹)	ΔG_b (kJmol ⁻¹)
3.61	201	-32.25	4.33	-20.75

3.9. Assembling of Fe₃O₄/SiO₂/Cu NPs in the micelles of CTAB

The dynamic nature of solubilization caused the Fe₃O₄/SiO₂/Cu NPs to stay for a different time in the exterior and interior of micelles and this affected UV-Vis absorbance, thus we witnessed random absorptions. The degree of solubilization and plausible location of Fe₃O₄/SiO₂/Cu NPs in CTAB micelles was directly related to temperature, the concentration of the participating additives and surfactant, chemical and structural nature of additive molecules. The location and mechanism of the process rely on quantitative values of partition constant and partitioning coefficient within micellar and aqueous phases. Higher values of K_x directed the Fe₃O₄/SiO₂/Cu NPs to accommodate in the palisade layer of micelles.

The higher the value of K_x , the greater tendency of transference of Fe₃O₄/SiO₂/Cu NPs towards the outer region of micellar media due to the interaction of carboxylic negative charge and cationic head of CTAB. The values of partition coefficient K_x (201×10^3) in the micelles were significantly higher as compared to K_b (4.33×10^3 dm³mol⁻¹). This system was stable and partitioning of Fe₃O₄/SiO₂/Cu NPs was spontaneous as indicated by negative values of ΔG_p (-32.25 kJmol⁻¹) and ΔG_b (-20.75 kJmol⁻¹) as summarized in Table 2. Based on partitioning attributes, the possible locus of Fe₃O₄/SiO₂/Cu NPs in the micelles of CTAB is presented in Figure 11.

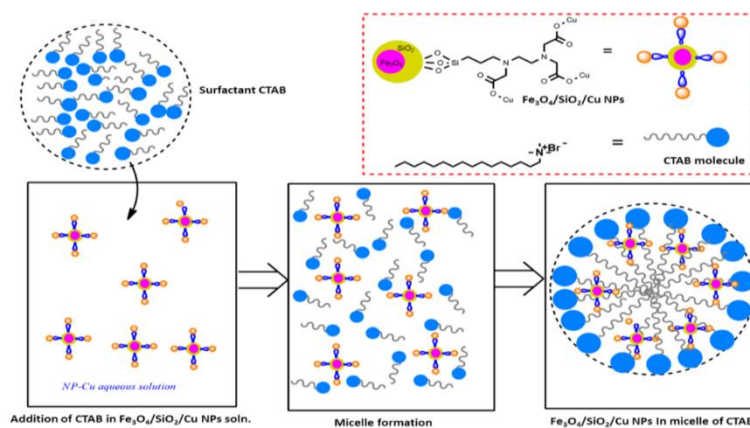


Fig. 11. Partitioning and locus of $\text{Fe}_3\text{O}_4/\text{SiO}_2/\text{Cu}$ NPs in the micelles of CTAB.

3.10. Photo antibacterial properties

The results of the tests performed on *S. aureus* exposed to UV light sources are shown in Fig. 12A. The control group showed very small growth as compared to $\text{Fe}_3\text{O}_4/\text{SiO}_2/\text{Cu}$ NPs. The results of the sample exposed to a visible light source and under dark conditions are illustrated in Fig. 12B and 12C. As presented in Fig. 12B, the control group showed a significant increase in bacterial growth over time, but the presence of $\text{Fe}_3\text{O}_4/\text{SiO}_2/\text{Cu}$ NPs prevented bacterial growth.

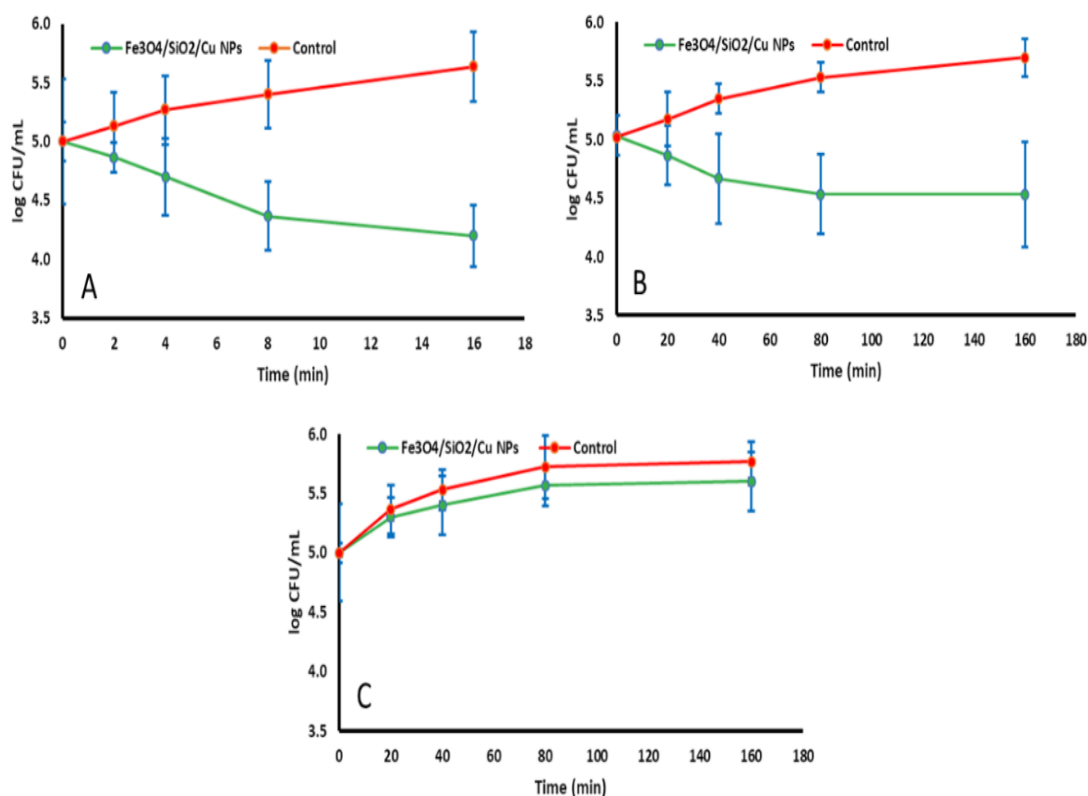


Fig. 12. The reduction in cell viability of $\text{Fe}_3\text{O}_4/\text{SiO}_2/\text{Cu}$ NPs and control samples for *S. aureus*: (A) *S. aureus* exposed to UV light, (B) *S. aureus* after exposure to visible light, and (C) *S. aureus* in darkness.

The bacterial growth in all samples under dark conditions demonstrated light dependence of antibacterial properties. The photo-antibacterial examination of *E. coli* in the UV light, visible light and dark conditions are shown in Fig. 13A, 13b and 13C correspondingly. In Fig. 13A it is very clear that the decline in colony count is attributed to $\text{Fe}_3\text{O}_4/\text{SiO}_2/\text{Cu}$ NPs and comparatively the control group showed no significant change. The control group experienced significant bacterial growth under visible light could be seen in Fig. 13B, whereas the presence of $\text{Fe}_3\text{O}_4/\text{SiO}_2/\text{Cu}$ NPs caused the highest decrease in growth. All the samples under dark conditions experienced growth in darkness with time (Fig. 13C). This trend highlighted the role and significance of the importance of light in reaction systems.

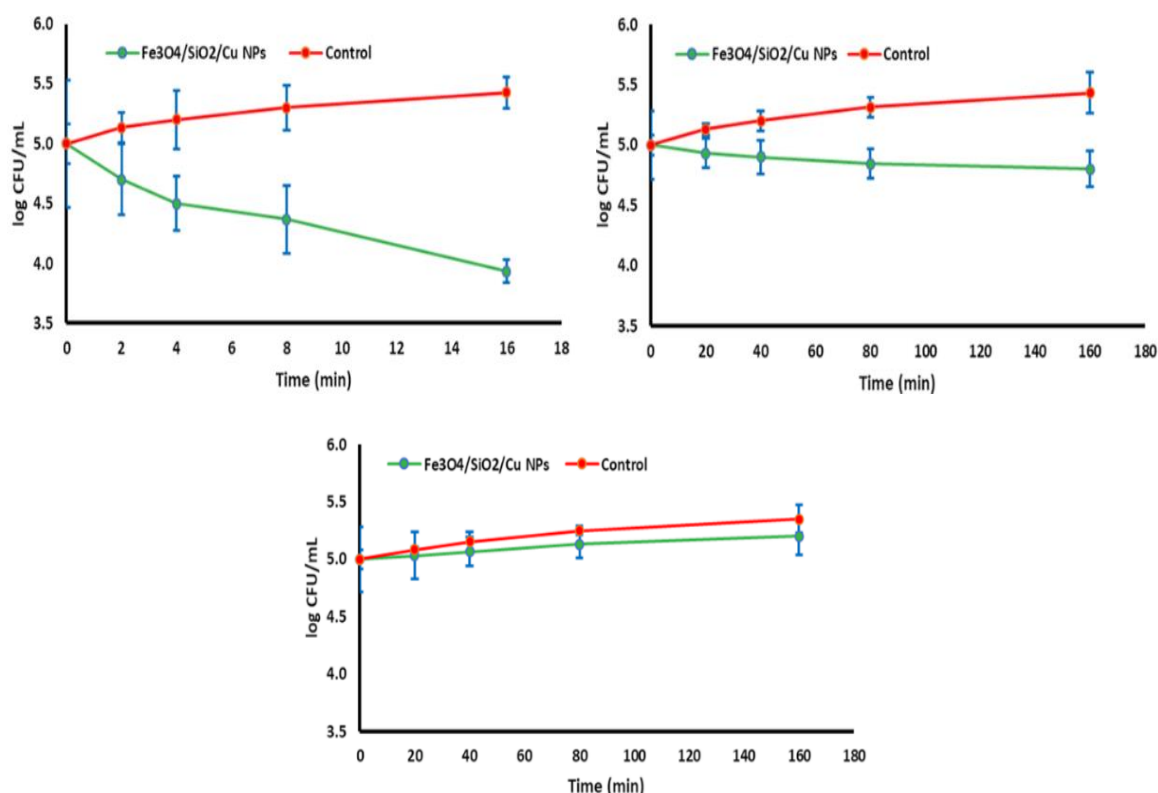


Fig. 13. The reduction in cell viability of $\text{Fe}_3\text{O}_4/\text{SiO}_2/\text{Cu}$ NPs and control samples for *E. coli*: (A) *E. coli* exposed to UV light, (B) *E. coli* after exposure to visible light, and (C) *E. coli* without light access.

4. Conclusions

$\text{Fe}_3\text{O}_4/\text{SiO}_2/\text{Cu}$ NPs were successfully synthesized via the modified Stober method. Thermodynamic studies demonstrate the increases in the critical CMC of surfactant due to the incorporation of the $\text{Fe}_3\text{O}_4/\text{SiO}_2/\text{Cu}$ NPs in the micelles. From experimental findings, it was noticed that the value of critical micelle concentration in the $\text{Fe}_3\text{O}_4/\text{SiO}_2/\text{Cu}$ NPs/CTAB system was higher than pure CTAB. The CMC of pure CTAB shifted from 0.9 mM to 0.914 mM as revealed by conductivity data and to 0.917 mM as indicated by UV-Vis analysis. The photo antibacterial studies on *E. coli* and *S. aureus* by $\text{Fe}_3\text{O}_4/\text{SiO}_2/\text{Cu}$ NPs under dark conditions, UV,

and visible light irradiation showed that the optimized nanoparticles have a good antibacterial impact.

Acknowledgements

All authors are thankful to The Islamia University Bahawalpur, Bahawalpur Pakistan for providing the necessary facilities to conduct this research work.

References

1. E. Routoula and S.V. Patwardhan: Degradation of anthraquinone dyes from effluents: a review focusing on enzymatic dye degradation with industrial potential *Environmental science & technology*. 54(2), 647 (2020); <https://doi.org/10.1021/acs.est.9b03737>
2. M. I Litter and N. Quici: Photochemical advanced oxidation processes for water and wastewater treatment *Recent Patents on Engineering*. 4(3), 217 (2010); <https://doi.org/10.2174/187221210794578574>
3. S. Aroob, M.B. Taj, S. Shabbir, M. Imran, R.H. Ahmad, S. Habib, A. Raheel, M.N. Akhtar, M. Ashfaq and M. Sillanpää: In situ biogenic synthesis of CuO nanoparticles over graphene oxide: A potential nanohybrid for water treatment *Journal of Environmental Chemical Engineering*. 9(4), 105590 (2021); <https://doi.org/10.1016/j.jece.2021.105590>
4. F. Ahmad, M.B. Taj, M. Ramzan, H. Ali, A. Ali, M. Adeel, H.M. Iqbal and M. Imran: One-pot synthesis and characterization of in-house engineered silver nanoparticles from *Flacourtia jangomas* fruit extract with effective antibacterial profiles *Journal of Nanostructure in Chemistry*. 11(1), 131 (2021); <https://doi.org/10.1007/s40097-020-00354-w>
5. H. Ghasemi, B. Aghabarari, M. Alizadeh, A. Khanlarkhani and N. Abu-Zahra: High efficiency decolorization of wastewater by Fenton catalyst: Magnetic iron-copper hybrid oxides *Journal of Water Process Engineering*. 37, 101540 (2020); <https://doi.org/10.1016/j.jwpe.2020.101540>
6. F.J. Contesini, R.R.d. Melo and H.H. Sato: An overview of *Bacillus proteases*: from production to application *Critical reviews in biotechnology*. 38(3), 321 (2018); <https://doi.org/10.1080/07388551.2017.1354354>
7. X.-G. Zhang, D.-L. Guan, C.-G. Niu, Z. Cao, C. Liang, N. Tang, L. Zhang, X.-J. Wen and G.-M. Zeng: Constructing magnetic and high-efficiency AgI/CuFe₂O₄ photocatalysts for inactivation of *Escherichia coli* and *Staphylococcus aureus* under visible light: Inactivation performance and mechanism analysis *Science of the total environment*. 668, 730 (2019); <https://doi.org/10.1016/j.scitotenv.2019.03.068>
8. A. Kubacka, M.S. Diez, D. Rojo, R. Bargiela, S. Ciordia, I. Zapico, J.P. Albar, C. Barbas, V.A.M. dos Santos and M. Fernández-García: Understanding the antimicrobial mechanism of TiO₂-based nanocomposite films in a pathogenic bacterium *Scientific reports*. 4(1), 1 (2014); <https://doi.org/10.1038/srep04134>
9. L. Wang, P. Jin, S. Duan, H. She, J. Huang and Q. Wang: In-situ incorporation of Copper (II) porphyrin functionalized zirconium MOF and TiO₂ for efficient photocatalytic CO₂ reduction *Science Bulletin*. 64(13), 926 (2019); <https://doi.org/10.1016/j.scib.2019.05.012>
10. S. Mohammadi-Aghdam, B. Sarkhosh and N.N. Tajoddin: Recyclable Fe₃O₄/SiO₂/TiO₂/Cu nanocomposites: synthesis, characterization and investigation of the photocatalytic and magnetic property *J. Mater. Sci. Mater. Electron*. 28, 9456 (2017); <https://doi.org/10.1007/s10854-017-6688-x>
11. M.A. Marsooli, M. Rahimi-Nasrabadi, M. Fasihi-Ramandi, K. Adib, M. Eghbali-Arani, F. Ahmadi, E. Sohoul, S.A. Mirhosseini, M.R. Gangali and H. Ehrlich: Preparation of Fe₃O₄/SiO₂/TiO₂/CeVO₄ nanocomposites: investigation of photocatalytic effects on organic pollutants, bacterial environments, and new potential therapeutic candidate against cancer cells

- Frontiers in pharmacology. 11, 192 (2020); <https://doi.org/10.3389/fphar.2020.00192>
12. M. Taj, A. Raheel, W. Alelwani, D. Hajjar, A. Makki, A. Alnajeebi, N. Babteen, S. Tirmizi and S. Noor: A Swift One-Pot Solvent-Free Synthesis of Benzimidazole Derivatives and Their Metal Complexes: Hydrothermal Treatment, Enzymatic Inhibition, and Solubilization Studies Russian Journal of General Chemistry. 90(8), 1533 (2020); <https://doi.org/10.1134/S107036322008023X>
13. S. Noor, N. Younas, M.A. Rashid, S. Nazir, M. Usman and T. Naz: Spectroscopic, conductometric and biological investigation of [Ni (phen) 3] F2. EtOH. MeOH. 8H2O complex in anionic micellar media Colloid and Interface Science Communications. 27, 26 (2018); <https://doi.org/10.1016/j.colcom.2018.09.004>
14. S. Noor and M.B. Taj: Mixed-micellar approach for enhanced dye entrapment: A spectroscopic study Journal of Molecular Liquids. 338, 116701 (2021); <https://doi.org/10.1016/j.molliq.2021.116701>
15. S. Noor, M.B. Taj and A. Ashar: Solubilization of cationic dye in single and mixed micellar media Journal of Molecular Liquids. 330, 115613 (2021); <https://doi.org/10.1016/j.molliq.2021.115613>
16. M.B. Taj, M.D. Alkahtani, U. Ali, A. Raheel, W. Alelwani, A.M. Alnajeebi, N.A. Babteen, S. Noor and H. Alshater: New heteroleptic 3D metal complexes: synthesis, antimicrobial and solubilization parameters Molecules. 25(18), 4252 (2020); <https://doi.org/10.3390/molecules25184252>
17. N. Younas, M.A. Rashid, M. Usman, S. Nazir, S. Noor, A. Basit and M. Jamil: Solubilization of Ni imidazole complex in micellar media of anionic surfactants, sodium dodecyl sulfate and sodium stearate Journal of Surfactants and Detergents. 20(6), 1311 (2017); <https://doi.org/10.1007/s11743-017-1997-x>
18. M.M. Aafreen, R. Anitha, R.C. Preethi, S. Rajeshkumar and T. Lakshmi: Anti-Inflammatory activity of silver nanoparticles prepared from ginger oil-an invitro approach Indian Journal of Public Health Research & Development. 10(7), 145 (2019); <https://doi.org/10.5958/0976-5506.2019.01552.3>
19. J. Chambers, J.M. Stokes and R. Stokes: Conductances of concentrated aqueous sodium and potassium chloride solutions at 25 The Journal of Physical Chemistry. 60(7), 985 (1956); <https://doi.org/10.1021/j150541a040>
20. T. Shedlovsky: The electrolytic conductivity of some uni-univalent electrolytes in water at 25 Journal of the American Chemical Society. 54(4), 1411 (1932); <https://doi.org/10.1021/ja01343a020>
21. A. Maximenko, J. Depciuch, N. Łopuszyńska, M. Stec, Ż. Światkowska-Warkocka, V. Bayev, P.M. Zieliński, J. Baran, J. Fedotova and W.P. Węglarz: Fe 3 O 4@ SiO 2@ Au nanoparticles for MRI-guided chemo/NIR photothermal therapy of cancer cells RSC Advances. 10(44), 26508 (2020); <https://doi.org/10.1039/D0RA03699D>
22. J. Ramyadevi, K. Jeyasubramanian, A. Marikani, G. Rajakumar, A.A. Rahuman, T. Santhoshkumar, A.V. Kirthi, C. Jayaseelan and S. Marimuthu: Copper nanoparticles synthesized by polyol process used to control hematophagous parasites Parasitology research. 109(5), 1403 (2011); <https://doi.org/10.1007/s00436-011-2387-3>
23. H. Kawamura, M. Manabe, Y. Miyamoto, Y. Fujita and S. Tokunaga: Partition coefficients of homologous. omega.-phenylalkanols between water and sodium dodecyl sulfate micelles The Journal of Physical Chemistry. 93(14), 5536 (1989); <https://doi.org/10.1021/j100351a042>